

Efficient Estimation of Non-Circular (NC) Wavefronts via R -D Tensorized NC Tensor-ESPRIT-type Algorithms

Sai Pavan Deram ^{*†}, Khaled Ardah ^{‡§}, Joerg Widmer ^{*}, Martin Haardt[§]

^{*} IMDEA Networks Institute, [†] Universidad Carlos III Madrid, [‡] Lenovo Inc, [§] TU Ilmenau

Abstract—Subspace-based methods for R -D harmonic retrieval with non-circular (NC) sources provide advantages like improved resolution but face high computational demands. To address this, we propose a tensor-based framework that directly structures the augmented measurement tensor inherent to NC sources. We develop two variants: R -D Tensorized NC Tensor ESPRIT (Non-Circular Standard Tensor ESPRIT) and its real-valued counterpart R -D Tensorized NC Unitary Tensor ESPRIT (Non-Circular Unitary Tensor ESPRIT). Our complexity analysis reveals that R -D Tensorized NC Tensor ESPRIT reduces the computations by $\frac{R-1}{R} * 100\%$ (75% for $R=4$) compared to existing NC R -D ESPRIT methods by leveraging a unified higher dimensional structure with NC sources. Simulations confirm that R -D Tensorized NC Unitary Tensor ESPRIT retains the benefits of NC signal processing—enhanced resolution and identifiability—while achieving comparable accuracy to standard approaches at a significantly reduced computational cost.

I. INTRODUCTION

Direction-of-arrival (DOA) estimation is an important problem in array signal processing with applications in many fields, including wireless communications, radar, and sonar. Among various solutions, subspace-based methods (e.g., MUSIC (Multiple Signal Classification) [1] and ESPRIT (Estimation of Signal Parameters via Rotational Invariance Techniques) [2]) provide a good balance between estimation accuracy and computational complexity, e.g., compared to compressed sensing (CS)-based methods [3]. These methods, i.e., MUSIC and ESPRIT, rely on the decomposition of the spatial covariance matrix into signal and noise subspaces to estimate the spatial DoA parameters. Compared to MUSIC, ESPRIT is practically more attractive due to its computational efficiency, as it exploits the rotation invariance property of sensor arrays and avoids the exhaustive spectral search required by MUSIC. An extension of subspace-based DoA estimation methods for non-circular (NC) sources allows to exploit further statistical properties embedded in the source signals. By exploiting strictly NC sources, the aperture of the array can essentially be increased by a factor of 2, resulting in an improved estimation accuracy without the need for additional sensors. Work on exploiting NC sources for DoA estimation began with ESPRIT-like algorithms tailored for strictly non-circular signals [4], [5], which demonstrated much better computational efficiency by operating on real-valued matrices and improved resolution by virtually doubling the number of antenna elements. Subsequently, [6] introduced

improvements of MUSIC for NC sources. In [7], an IV-SSF framework for temporally and spatially correlated NC sources was proposed. Subsequent developments were gridless methods such as atomic norm minimization (ANM) for strictly NC sources in sparse array cases [8]. These methods bypassed grid discretization errors while achieving super-resolution performance.

Although classical subspace methods like ESPRIT were first mainly proposed for 1-D parameter estimation, there are also multi-dimensional extensions such as R -D Standard Tensor ESPRIT [9], R -D Unitary ESPRIT [10], R -D MUSIC [11], R -D MDF [12], R -D RARE [13], to tackle multi-parameter scenarios (e.g., azimuth, elevation, and delay). For example, in a 3-D parameter estimation problem ($R = 3$), the goal is to simultaneously estimate the azimuth (ϕ), elevation (θ), and delay (τ) parameters of the dominant paths. This is performed using rotational invariances in all 3D dimensions by using a 3D array geometry. Recently, these algorithms have been extended to explicitly exploit NC sources.

R -D techniques can outperform conventional methods in harmonic retrieval through simultaneous parameter estimation, noise robustness, and increasing degrees of freedom and resolution. However, the computational challenge (with NC sources) is still a major issue. Doubling the number of sensors and stacking the measurement matrices along the r -th dimension leads to a significantly higher computational overhead, since subspace estimation is expensive in each dimension.

Contributions. In order to preserve the advantages of R -D methods and NC sources, but to significantly reduce the computational burden, we structure the problem to represent an augmented measurement tensor by exploiting the structure in NC sources. The main contributions of our work are as follows:

- We derive an efficient signal model by leveraging the inherent higher-dimensional structure of NC sources, which consolidates multiple R -dimensional augmentations into a unified higher dimensional framework. Building on this framework, we propose the R -D Tensorized NC Tensor ESPRIT algorithm.
- Inspired by [14], we fully realize the real-valued implementation of R -D Tensorized NC Tensor ESPRIT, yielding a model that we call R -D Tensorized NC Unitary Tensor ESPRIT, which naturally integrates forward-

backward averaging. We provide detailed formulations and proofs for the real-valued transformation.

- We provide a detailed complexity analysis of R -D Tensorized NC Tensor ESPRIT and R -D Tensorized NC Unitary Tensor ESPRIT with respect to existing R -D ESPRIT variants.
- Through extensive simulations, we validate that the proposed R -D Tensorized NC Tensor ESPRIT and R -D Tensorized NC Unitary Tensor ESPRIT algorithms maintain a similar performance to existing R -D methods, with a $\frac{R-1}{R} \times 100\%$ reduction in computational complexity.

II. BACKGROUND AND NOTATION

This paper employs the following mathematical notation: scalars are denoted by italic letters (e.g., A , a), vectors by bold lowercase letters (e.g., \mathbf{a}), and matrices by bold uppercase letters (e.g., \mathbf{A}). Key operators include the Kronecker product (\otimes), Khatri-Rao product (\diamond), Hadamard product (\odot), matrix transpose (\cdot^T), conjugate (\cdot^*), Hermitian transpose (\cdot^H), and Moore-Penrose pseudoinverse (\cdot^\dagger). Finally, $\mathbf{1}_K \in \mathbb{R}^{K \times 1}$ and $\mathbf{0}_K \in \mathbb{R}^{K \times 1}$ are the vectors of ones and zeros, respectively. The Frobenius norm and the higher order norm are represented by $\|\cdot\|_F$ and $\|\cdot\|_H$, respectively.

Tensors denoted as bold calligraphic letters (e.g., \mathcal{A}) are multiway arrays. The major advantage of using tensors is their ability to preserve and reveal the inherent multi-modal structure of data, leading to more interpretable and physically meaningful models. For a R -way tensor $\mathcal{A} \in \mathbb{C}^{M_1 \times \dots \times M_R}$, its r -mode unfolding is written as $[\mathcal{A}]_{(r)}$. Given a matrix $U_r \in \mathbb{C}^{J \times M_r}$ ($r \in \{1, \dots, R\}$), the r -mode product $\mathcal{Y} = \mathcal{A} \times_r U_r$ satisfies the unfolding relationship $[\mathcal{Y}]_{(r)} = U_r [\mathcal{A}]_{(r)}$. The repeated r -mode products of a tensor with matrices are denoted by the notation $\times_{r=1}^R$. The concatenation of two tensors along the r -th mode is denoted as $[\mathcal{A} \sqcup_r \mathcal{B}]$. The following properties will be used in the rest of the paper [15].

$$[\mathcal{A} \sqcup_r \mathcal{B}] \times_p U_p = [\mathcal{A} \times_p U_p \sqcup_r \mathcal{B} \times_p U_p], \forall r \neq p \quad (1)$$

$$[\mathcal{A} \sqcup_r \mathcal{B}] \times_r [U_r \mathbf{W}_r] = \mathcal{A} \times_r U_r + \mathcal{B} \times_r \mathbf{W}_r \quad (2)$$

$$\mathcal{A} \times_r \begin{bmatrix} \mathbf{X}_r \\ \mathbf{Y}_r \end{bmatrix} = [\mathcal{A} \times_r \mathbf{X}_r \sqcup_r \mathcal{A} \times_r \mathbf{Y}_r] \quad (3)$$

The PARAFAC (Parallel Factor Analysis), also known as CANDECOMP/PARAFAC decomposition (CPD), is a fundamental tensor factorization technique. In the CPD model, a tensor is expressed as a sum of rank-one tensors, where each component is formed by the outer product of vectors from each mode. For example, a third-order tensor $\mathcal{X} \in \mathbb{R}^{I \times J \times K}$ of rank R can be decomposed as

$$\begin{aligned} \mathcal{X} &= \sum_{r=1}^R \mathbf{a}_r \circ \mathbf{b}_r \circ \mathbf{c}_r \\ &= \mathcal{I}_{3,R} \times_1 \mathbf{A} \times_2 \mathbf{B} \times_3 \mathbf{C}, \end{aligned}$$

where \circ denotes the outer product and the vectors \mathbf{a}_r , \mathbf{b}_r , and \mathbf{c}_r are the factors in each mode. Consider a tensor $\mathcal{X} \in \mathbb{C}^{M_1 \times \dots \times M_R \times N}$. Its HOSVD is given by [16]

$$\mathcal{X} = \mathcal{S} \times_1 \mathbf{U}_1 \times_2 \mathbf{U}_2 \times_3 \dots \times_R \mathbf{U}_R, \quad (4)$$

where \mathcal{S} is the core tensor, and $\mathbf{U}_r \in \mathbb{C}^{M_r \times M_r}$ are orthogonal matrices representing the subspaces of each mode.

III. SIGNAL MODEL

Consider a separable R -dimensional array with dimensions $M = M_1 \times \dots \times M_R$, with narrowband far-field emitting sources that create planar wavefronts impinging on the array. The noisy R -dimensional measurements for an antenna array with an arbitrary phase reference can be represented as follows

$$\mathcal{Y} = \mathcal{A} \times_{R+1} \mathcal{S}^T + \mathcal{N} \in \mathbb{C}^{M_1 \times M_2 \times \dots \times M_R \times N}, \quad (5)$$

where the $\mathcal{S} \in \mathbb{C}^{d \times N}$ contains N snapshots from each of the d sources. The tensor \mathcal{N} models additive noise at every one of the M antenna elements with zero mean and the variance σ^2 . The tensor $\mathcal{A} \in \mathbb{C}^{M_1 \times \dots \times M_R \times d}$ is the array steering tensor with the following structure

$$\mathcal{A} = \mathcal{I}_{R,d} \times_1 \mathbf{A}_1 \times_2 \dots \times_R \mathbf{A}_R \in \mathbb{C}^{M_1 \times \dots \times M_R \times d}. \quad (6)$$

The r -th factor matrix ($\mathbf{A}_r, \forall r \in \{1, \dots, R\}$) is the collection of the array response vectors ($\mathbf{a}^{(r)}(\mu_i), \forall i \in \{1, \dots, d\}$) where each vector $\mathbf{a}^{(r)}(\mu_i)$

$$\mathbf{a}^{(r)}(\mu_i^{(r)}) = \left[1, e^{j\mu_i^{(r)}}, \dots, e^{j(M_r-1)\mu_i^{(r)}} \right]^T.$$

depends on spatial frequency $\mu_i^{(r)}$ in the r -th dimension. It is important to note that the factor matrices in eqn. (6) do not have to conform to a Vandermonde structure. Instead, they must satisfy a shift-invariance property as in eqn. (8) as explained in [17]. For notational simplicity, we assume these matrices exhibit a symmetry property through the relationship

$$\mathbf{\Pi}_{M_r} \mathbf{A}_r^* = \mathbf{A}_r \mathbf{\Delta}_r, \quad \text{where} \quad (7)$$

the matrix $\mathbf{\Pi}_M \in \mathbb{R}^{M \times M}$ is an exchange matrix with ones on its antidiagonal and zeros elsewhere, and $\mathbf{\Delta}_r = \text{diag}\{\delta_r\} \in \mathbb{C}^{d \times d}$ is a unitary diagonal matrix. Note that this centrosymmetry of the array is not necessary as explained in [17]. The primary goal here is to estimate the d spatial frequency vectors

$$\boldsymbol{\mu}_i = \left[\mu_i^{(1)} \dots \mu_i^{(R)} \right]^T, i = 1, \dots, d$$

corresponding to R -dimensional signals exploiting the shift invariance along each mode of the array as follows:

$$\mathcal{A} \times_r \mathbf{J}_1^{(r)} \times_{R+1} \mathbf{\Phi}^{(r)} = \mathcal{A} \times_r \mathbf{J}_2^{(r)}, \forall r \quad (8)$$

where $\mathbf{\Phi}^{(r)} = \text{diag}\{[e^{j\mu_1^{(r)}}, \dots, e^{j\mu_d^{(r)}}]\}$ contains phase shifts and $\mathbf{J}_1^{(r)}, \mathbf{J}_2^{(r)}$ are selection matrices defined as

$$\mathbf{J}_1^{(r)} = [\mathbf{I}_{M_r-1} \mathbf{0}_{M_r-1 \times 1}], \mathbf{J}_2^{(r)} = [\mathbf{0}_{M_r-1 \times 1} \mathbf{I}_{M_r-1}]. \quad (9)$$

Strictly non-circular sources enable *virtual sensor doubling*, which increases array resolution without physical hardware expansion. This is achieved by the structure of the strictly NC symbol matrix \mathbf{S} , which satisfies [5]

$$\mathbf{S} = \mathbf{\Psi} \mathbf{S}_0, \quad \mathbf{S}_0 \in \mathbb{R}^{d \times N}, \quad (10)$$

where $\mathbf{\Psi} = \text{diag}\{[e^{j\psi_1}, \dots, e^{j\psi_d}]\} \in \mathbb{C}^{d \times d}$ contains arbitrary phase shifts. For a R -D array, sensor doubling is applied independently to each mode in [10], [17]. The augmented measurement tensor for the r -th mode, $\mathbf{y}^{(\text{nc}, r)} \in \mathbb{C}^{M_1 \times \dots \times 2M_r \times \dots \times M_R \times N}$, is constructed as [10]:

$$\mathbf{y}^{(\text{nc}, r)} = \left[\mathbf{y} \sqcup_r \mathbf{y}^* \times_{r=1}^R \mathbf{\Pi}_{M_r} \right], \quad (11)$$

where $\mathbf{\Pi}_{M_r}$ is the exchange matrix. While doubling the sensor along the r -th mode (to $2M_r$) improves the resolution, it inherently increases the computational complexity due to the higher dimensional subspace estimation required for each mode. This trade-off is particularly pronounced in multidimensional arrays, where the subspace estimation must be repeated independently for each mode.

IV. PROPOSED FRAMEWORK

Unlike the conventional approach [10], [17] presented in eqn. (11), we propose to redefine the augmented measurement tensor by defining an additional tensor dimension (mode $(R+2)$). The resulting measurement tensor $\mathbf{y}^{(\text{nc})} \in \mathbb{C}^{M_1 \times \dots \times M_R \times N \times 2}$ is constructed as

$$\mathbf{y}^{(\text{nc})} = \left[\mathbf{y} \sqcup_{R+2} \mathbf{y}^* \times_{r=1}^R \mathbf{\Pi}_{M_r} \right]. \quad (12)$$

The additional dimension of size two along mode $(R+2)$ is a result of sensor doubling across all the array modes that arises from the characteristics of strictly NC sources.

To this end, we show the following key properties.

1. **Shift Invariance Preservation:** The augmented steering tensor must preserve shift invariance, a requirement for ESPRIT-type algorithms. This property ensures that the augmented tensor structure supports direct parameter estimation via shift-invariance relations, even when the original array lacks a centro-symmetric geometry.

2. **CP structure and rank:** While the component tensors in equation (12) individually correspond to the CP structure with rank d (as confirmed by the equations (5) and (6)), concatenation along a new mode does not inherently preserve the CP structure [18]. This operation can increase the effective rank beyond d [19], potentially compromising source separability and estimation accuracy. These properties underscore the need for rigorous theoretical analysis to ensure structural integrity during tensor augmentation, while balancing resolution and computational efficiency.

To address these challenges, we propose the following lemma.

Lemma 1. *Let \mathbf{A} and \mathbf{B} be two CP tensors of the same size and rank L , where all factors of \mathbf{B} are column-scaled*

versions of \mathbf{A} . If these tensors are concatenated along the r -th dimension, then the resulting higher-order $(R+1)$ -D tensor \mathbf{C} retains a CP structure. The factor matrix for the new mode will be a $2 \times d$ matrix, where each column represents the scaling of the r -th component in the first and second tensor, respectively.

Proof. Let the tensors be defined as

$$\begin{aligned} \mathbf{A} &= \mathcal{I}_{R,l} \times_1 \mathbf{F}_1 \times_2 \dots \times_R \mathbf{F}_R \\ \mathbf{B} &= \mathcal{I}_{R,l} \times_1 \mathbf{F}_1 \mathbf{E}_1 \times_2 \dots \times_R \mathbf{F}_R \mathbf{E}_R \\ \mathbf{C} &= [\mathbf{A} \sqcup_r \mathbf{B}], \forall r = 1, \dots, R \end{aligned}$$

and $\mathbf{E}_r = \text{diag}\{e_r\}$ be diagonal scaling matrices. Let us rewrite the tensor \mathbf{B} as a $(R+1)$ -D tensor

$$\begin{aligned} \mathbf{B} &= \mathcal{I}_{R,l} \times_1 \mathbf{F}_1 \mathbf{E}_1 \times_2 \dots \times_R \mathbf{F}_R \mathbf{E}_R \\ &= \mathcal{I}_{R,l} \times_1 (e_1^T \diamond \mathbf{F}_1) \times_2 \dots \times_R (e_R^T \diamond \mathbf{F}_R) \\ &= \mathcal{I}_{R+1,l} \times_1 \mathbf{F}_1 \times_2 \dots \times_R \mathbf{F}_R \times_{R+1} (e_1^T \odot \dots \odot e_R^T) \\ &= \mathbf{A} \times_{R+1} (e_1^T \odot \dots \odot e_R^T). \end{aligned}$$

Similarly, \mathbf{A} can be written as

$$\mathbf{A} = \mathcal{I}_{R+1,l} \times_1 \mathbf{F}_1 \times_2 \dots \times_R \mathbf{F}_R \times_{R+1} \mathbf{1}_l^T.$$

Using the above two results and eqn. (3), the resulting tensor \mathbf{C} can be written as

$$\begin{aligned} \mathbf{C} &= [\mathbf{A} \times_{R+1} \mathbf{1}_l^T \sqcup_r \mathbf{A} \times_{R+1} (e_1^T \odot \dots \odot e_l^T)] \\ &= \mathbf{A} \times_{R+1} \mathbf{F}_{R+1}, \end{aligned}$$

where $\mathbf{F}_{R+1} = \left[(e_1^T \odot \dots \odot e_R^T) \right] \in \mathbb{C}^{2 \times l}$. In the resulting tensor \mathbf{C} , the new mode's factor matrix is of rank 2, but the overall tensor's rank still remains the l . \square

Using the above result, the augmented measurement tensor $\mathbf{y}^{(\text{nc})} \in \mathbb{C}^{M_1 \times \dots \times M_R \times N \times 2}$ in eqn. (12) can be expressed as:

$$\begin{aligned} \mathbf{y}_0^{(\text{nc})} &= \mathcal{I}_{R+2,d} \times_1 \mathbf{A}_1 \times_2 \dots \times_R \mathbf{A}_R \times_{R+1} \mathbf{S}_0^T \times_{R+2} \mathbf{\Xi} \\ \mathbf{y}^{(\text{nc})} &= \mathbf{y}_0^{(\text{nc})} + \tilde{\mathcal{N}} \end{aligned} \quad (13)$$

where

$$\mathbf{A}^{(\text{nc})} = \mathcal{I}_{R+2,d} \times_1 \mathbf{A}_1 \times_2 \dots \times_{R+1} \mathbf{I}_d \times_{R+2} \mathbf{\Xi}, \quad (14)$$

$\mathbf{y}_0^{(\text{nc})}$ is the noiseless measurement tensor. Here, $\mathbf{\Xi} \in \mathbb{C}^{2 \times d}$ and takes the form

$$\mathbf{\Xi} = \left[(\delta_1^T \odot \dots \odot \delta_R^T \odot \psi^H) \right] \in \mathbb{C}^{2 \times d}. \quad (15)$$

The arbitrary phase shifts ψ and δ_r are inherent properties of strictly NC sources (eqn. (10)) and the mode-specific array geometries (eqn.(7)), respectively. If the phase reference is at the center of the r -th array, the phase shift matrix $\mathbf{\Delta}_r$ simplifies to the identity matrix ($\mathbf{\Delta}_r = \mathbf{I}_d$). Consequently, the augmented factor matrix along the new mode reduces to: $\mathbf{\Xi} = [\psi \quad \psi^*]^T$, where $\psi \in \mathbb{C}^d$ represents the NC phase shifts of the sources and contains the diagonal elements of the matrix $\mathbf{\Psi}$. This representation of the augmented measurement tensor in eqn. (13) captures the structure of the R -D array

and the NC measurements in a higher-dimensional space, enabling a compact representation and efficient processing. Furthermore, in eqn. (14), $\mathcal{A}^{(\text{nc})}$ is augmented the steering tensor derived by effectively doubling the number of antennas as a concatenation along the $(R+2)$ -th mode

$$\begin{aligned} \mathcal{A}^{(\text{nc})} &= \left[\mathcal{A} \times_{R+2} \psi^T \sqcup_{R+2} \mathcal{A}^* \times_{r=1}^R \Pi_{M_r} \times_{R+2} \psi^H \right] \\ &= \left[\mathcal{A}_1^{(\text{nc})} \sqcup_{R+2} \mathcal{A}_2^{(\text{nc})} \right], \text{ where,} \end{aligned} \quad (16)$$

$$\mathcal{A}_1^{(\text{nc})} = \mathcal{I}_{R+1,d} \times_1 \mathbf{A}_1 \times_2 \dots \times_{R+1} \mathbf{I}_d \times_{R+2} \psi^T \quad (17)$$

$$\begin{aligned} \mathcal{A}_2^{(\text{nc})} &= \mathcal{I}_{R+1,d} \times_1 \mathbf{A}_1 \times_2 \dots \times_{R+1} \mathbf{I}_d \\ &\quad \times_{R+2} (\delta_1^T \odot \dots \odot \delta_R^T \odot \psi^H). \end{aligned} \quad (18)$$

It is interesting to note that the two concatenated components of the tensor $\mathcal{A}^{(\text{nc})}$ are different from the original array manifold \mathcal{A} .

Property 1. *If the array steering tensor \mathcal{A} satisfies the R shift-invariant properties in eqn. (8), then $\mathcal{A}^{(\text{nc})}$ (14) is also shift-invariant and satisfies*

$$\mathcal{A}^{(\text{nc})} \times_r \mathbf{J}_1^{(r)} \times_{R+1} \Phi^{(r)} = \mathcal{A}^{(\text{nc})} \times_r \mathbf{J}_2^{(r)}, \forall r. \quad (19)$$

Proof. The proof is omitted due to space limitations. The shift invariance properties can be directly derived from the structure of $\mathcal{A}^{(\text{nc})}$ in eqn. (14) combined with the inherent shift invariance properties of the individual factor matrices \mathbf{A}_r . \square

V. PROPOSED R -D NC ESPRIT-TYPE ALGORITHMS

In this section, we present the R -D Tensorized NC Tensor ESPRIT and the R -D Tensorized NC Unitary Tensor ESPRIT algorithms for arbitrarily formed R -dimensional shift-invariant-structured array geometries.

A. R -D Tensorized NC Tensor ESPRIT

Subspace estimation is fundamental to ESPRIT algorithms, enabling high-resolution parameter estimation by leveraging the geometric structure of signal subspaces. For an R -dimensional measurement tensor $\mathcal{Y}^{(\text{nc})}$ containing d sources, the HOSVD is expressed as:

$$\mathcal{Y}^{(\text{nc})} = \mathcal{S} \times_1 \mathbf{U}_1 \dots \times_{R+1} \mathbf{U}_{R+1} \times_{R+2} \mathbf{U}_{R+2},$$

where \mathcal{S} represents the core tensor and $\mathbf{U}_r \in \mathbb{C}^{M_r \times M_r}$, $\forall r = 1, \dots, R$, $\mathbf{U}_{R+1} \in \mathbb{C}^{N \times N}$, $\mathbf{U}_{R+2} \in \mathbb{C}^{2 \times 2}$ are the unitary factor matrices corresponding to each mode. Let $\hat{\mathcal{U}}^{[s]}$ be the multidimensional subspace of the measurement tensor $\mathcal{Y}^{(\text{nc})}$ estimated by retaining the dominant d components:

$$\hat{\mathcal{U}}^{[s]} = \mathcal{S}^{[s]} \times_1 \mathbf{U}_1^{[s]} \dots \times_R \mathbf{U}_R^{[s]} \times_{R+2} \mathbf{U}_{R+2} \in \mathbb{C}^{M_1 \times M_2 \dots d \times 2}.$$

It has been shown that augmented steering vectors for d sources over R dimensions exhibit shift invariance in each of the modes. Since $\mathcal{A}^{(\text{nc})}$ and $\mathcal{Y}^{(\text{nc})}$ span identical column spaces, the unknown steering tensor in the shift invariance

equations eqn. (19) can be replaced by $\hat{\mathcal{U}}^{[s]}$. The resulting shift invariance equation for the r -th dimension is given as

$$\hat{\mathcal{U}}^{[s]} \times_r \mathbf{J}_1^{(r)} \times_{R+1} \Gamma^{(r)} \approx \hat{\mathcal{U}}^{[s]} \times_r \mathbf{J}_2^{(r)}, \forall r \quad (20)$$

where, $\Gamma^{(r)} = \mathbf{T}^{-1} \Phi^{(r)} \mathbf{T}$ and this follows from the fact that \mathcal{A} spans the same subspace $\mathcal{U}^{[s]}$ and $\mathcal{A} \approx \mathcal{U}^{[s]} \times_{R+1} \mathbf{T}$. The least squares solution to eqn. (20) is formulated as:

$$\Gamma^{(r)} = \arg \min_{\Gamma^{(r)}} \left\| \hat{\mathcal{U}}^{[s]} \times_r \mathbf{J}_1^{(r)} \times_{R+1} \Gamma^{(r)} - \hat{\mathcal{U}}^{[s]} \times_r \mathbf{J}_2^{(r)} \right\|_H, \quad (21)$$

yielding:

$$\hat{\Gamma}^{(r)} = \left(\tilde{\mathbf{J}}_1^{(r)} \cdot [\hat{\mathcal{U}}^{[s]}]_{(R+1)}^T \right)^\dagger \cdot \tilde{\mathbf{J}}_2^{(r)} \cdot [\hat{\mathcal{U}}^{[s]}]_{(R+1)}^T, \quad (22)$$

where $\tilde{\mathbf{J}}_i^{(r)} = \left(\mathbf{I}_2 \otimes \mathbf{I}_{M_1} \otimes \mathbf{I}_{M_2} \dots \mathbf{J}_i^{(r)} \dots \otimes \mathbf{I}_{M_R} \right)$, $i = 1, 2$. After independently solving the equation eqn. (21) for the matrix estimate $\hat{\Gamma}^{(r)}$ in each mode r , the properly paired spatial frequency estimates are obtained by the expression:

$$\hat{\mu}_i^{(r)} = \arg \left(\hat{\lambda}_i^{(r)} \right), \quad i = 1, \dots, d, \quad (23)$$

where $\hat{\lambda}_i^{(r)}$ are the eigenvalues of $\hat{\Gamma}^{(r)}$. These eigenvalues correspond to the rotational invariance property and are critical for estimating the spatial frequencies in each dimension. To ensure consistent parameter pairing across all R dimensions, the eigenvalues $\hat{\lambda}_i^{(r)}$ are computed using either a joint eigendecomposition across all dimensions or the simultaneous Schur decomposition.

B. R -D Tensorized NC Unitary Tensor ESPRIT

In this subsection, we extend the framework presented in [14] to handle the augmented measurement tensor $\mathcal{Y}^{(\text{nc})}$ and derive the R -D Tensorized NC Unitary Tensor ESPRIT algorithm. This adaptation consists of two significant preprocessing steps: 1. **Forward-Backward Averaging (FBA):** Used over $\mathcal{Y}^{(\text{nc})}$ to impose a centro-Hermitian structure, allowing us to achieve 2. **Real-Valued Transformation:** Unitary transformations take the complex tensor to real-valued data. While FBA typically improves the performance by effectively doubling snapshots, its role here is to enable real-valued transformation, not to improve the resolution for coherent sources. Let \mathcal{Z} be the tensor obtained by FBA as

$$\mathcal{Z} = \left[\mathcal{Y}^{(\text{nc})} \sqcup_{R+1} \left(\mathcal{Y}^{(\text{nc})} \times_{r=1}^R \Pi_{M_r} \right) \times_{R+1} \Pi_N \times_{R+2} \Pi_2 \right]$$

Using the symmetry property derived in Appendix A, the tensor \mathcal{Z} can be further simplified as

$$\mathcal{Z} = \left[\mathcal{Y}^{(\text{nc})} \sqcup_{R+1} \mathcal{Y}^{(\text{nc})} \times_{R+1} \Pi_N \right] \in \mathbb{C}^{M_1 \times \dots \times M_R \times 2N \times 2}.$$

The structure of \mathcal{Z} demonstrates that FBA does not alter the signal subspace of $\mathcal{Y}^{(\text{nc})}$. This invariance arises because \mathcal{Z} and $\mathcal{Y}^{(\text{nc})}$ span identical r -mode subspaces for $r = 1, 2, \dots, R$, implying that applying FBA introduces no additional information or constraints.

Property 2. (*Centro-Hermitian Property of FBA-Processed Tensor*) Let \mathcal{Z} be the tensor obtained after applying Forward Backward Averaging (FBA) to $\mathcal{X}^{(\text{nc})}$. Then, \mathcal{Z} is centro-Hermitian and satisfies:

$$\mathcal{Z}^* \times_{r=1}^R \Pi_{M_r} \times_{R+1} \Pi_{2N} \times_{R+2} \Pi_2 = \mathcal{Z},$$

Proof. The proof follows standard steps (see, e.g., [10]) and is omitted for brevity. \square

Since the tensor \mathcal{Z} is centro-Hermitian, it can be efficiently transformed into a real-valued representation using a structured unitary mapping. This is achieved via a bijective correspondence between the set of centro-Hermitian tensors and real-valued tensors, as established in [9]. Specifically, define a left Π -real matrix $\mathbf{Q}_p \in \mathbb{C}^{p \times p}$, which satisfies the symmetry condition: $\Pi_p \mathbf{Q}_p^* = \mathbf{Q}_p$. For example, the unitary matrix of odd order:

$$\mathbf{Q}_{2n} = \frac{1}{\sqrt{2}} \begin{bmatrix} \mathbf{I}_n & \mathbf{0}_{n \times 1} & j\mathbf{I}_n \\ \mathbf{0}_{n \times 1}^T & \sqrt{2} & \mathbf{0}_{n \times 1}^T \\ \Pi_n & \mathbf{0}_{n \times 1} & -j\Pi_n \end{bmatrix}$$

is left Π -real and enables the transformation to map \mathcal{Z} to a purely real tensor. A unitary left Π -real matrix of even order is obtained by dropping its center row and center column. This property is critical for such a transformation, where real-valued computations reduce complexity while preserving the shift-invariances,

Property 3. Given the centro-Hermitian property of \mathcal{Z} , we leverage a real-valued transformation of \mathcal{Z} , defined as:

$$\begin{aligned} \varphi(\mathcal{Z}) &= \left(\mathcal{Z} \times_{r=1}^R \mathbf{Q}_{M_r}^H \right) \times_{R+1} \mathbf{Q}_{2N}^H \times_{R+2} \mathbf{Q}_2^H \\ &= \left[\left[\text{Re}\{\mathcal{Q}\} \sqcup_{R+2} \text{Im}\{\mathcal{Q}\} \right] \sqcup_{(R+1)} \mathcal{O} \right], \end{aligned}$$

where $\mathcal{Q} = \mathcal{Y} \times_{r=1}^R \mathbf{Q}_{M_r}^H$ and $\mathcal{O} \in \mathbb{R}^{M_1 \times M_2 \times \dots \times M_R \times N}$ is a tensor containing only zeros.

Proof. The detailed derivation is provided in Appendix B. \square

The real-valued transformation of the tensor \mathcal{Z} is constructed by concatenating the real and imaginary components of the R -dimensional measurement tensor, followed by a mode-wise multiplication with left Π -real matrices ($\mathbf{Q}_{M_r}^H$) along each mode r . This transformation preserves the structural symmetry while enabling efficient real arithmetics. To this end, we define $\mathcal{D}^{(\text{nc})}$, the transformed steering tensor as

$$\mathcal{D}^{(\text{nc})} = \mathcal{A}^{(\text{nc})} \times_1 \mathbf{Q}_{M_1}^H \times \dots \times_R \mathbf{Q}_{M_R}^H.$$

Furthermore, $\mathcal{D}^{(\text{nc})}$ satisfies the shift-invariance properties

$$\mathcal{D}^{(\text{nc})} \times_r \mathbf{K}_1^{(r)} \times_{R+1} \Upsilon^{(r)} = \mathcal{D}^{(\text{nc})} \times_r \mathbf{K}_2^{(r)}, \forall r. \quad (24)$$

Here, $\mathbf{K}_1^{(r)}, \mathbf{K}_2^{(r)} \in \mathbb{C}^{(M_r-1) \times M_r}$ are transformed selection matrices [9] encoding subarray displacements defined as

$$\begin{aligned} \mathbf{K}_1^{(r)} &= 2 \cdot \text{Re} \left\{ \mathbf{Q}_{M_r-1}^H \mathbf{J}_2^{(r)} \mathbf{Q}_{M_r}^H \right\}, \\ \mathbf{K}_2^{(r)} &= 2 \cdot \text{Im} \left\{ \mathbf{Q}_{M_r-1}^H \mathbf{J}_2^{(r)} \mathbf{Q}_{M_r}^H \right\}, \end{aligned}$$

The multidimensional signal subspace $\hat{\mathcal{E}}^{[s]}$ of real valued measurement tensor $\varphi(\mathcal{Z})$ ignoring the zero tensor along the mode $R+1$ is estimated as

$$\hat{\mathcal{E}}^{[s]} = \mathcal{S}^{[s]} \times_1 \mathbf{E}_1^{[s]} \dots \times_R \mathbf{E}_R^{[s]} \times_{R+2} \mathbf{E}_{R+2} \in \mathbb{C}^{M_1 \times M_2 \times \dots \times d \times 2},$$

capturing the joint spatial, temporal, and non-circular characteristics of the signal. To estimate the spatial frequencies, the shift invariance property is enforced across each dimension $r = 1, \dots, R$, leading to the tensor equation

$$\hat{\mathcal{E}}^{[s]} \times_r \mathbf{K}_1^{(r)} \times_{R+1} \Upsilon^{(r)} \approx \hat{\mathcal{E}}^{[s]} \times_r \mathbf{K}_2^{(r)},$$

and $\Upsilon^{(r)} \in \mathbb{C}^{d \times d}$ contains phase factors. This is reformulated as a least squares problem:

$$\Upsilon^{(r)} = \arg \min_{\Upsilon^{(r)}} \left\| \hat{\mathcal{E}}^{[s]} \times_r \mathbf{K}_1^{(r)} \times_{R+1} \Upsilon^{(r)} - \hat{\mathcal{E}}^{[s]} \times_r \mathbf{K}_2^{(r)} \right\|_{\text{F}}.$$

The closed-form solution, obtained via the Moore-Penrose pseudo-inverse, is:

$$\Upsilon^{(r)} = \left(\tilde{\mathbf{K}}_1^{(r)} \cdot [\hat{\mathcal{E}}^{[s]}]_{(R+1)}^T \right)^\dagger \cdot \tilde{\mathbf{K}}_2^{(r)} \cdot [\hat{\mathcal{E}}^{[s]}]_{(R+1)}^T.$$

The matrices $\tilde{\mathbf{K}}_1^{(r)}$ and $\tilde{\mathbf{K}}_2^{(r)}$ are constructed using Kronecker products to isolate the r -th mode's shift-invariance:

$$\tilde{\mathbf{K}}_i^{(r)} = \left(\mathbf{I}_2 \otimes \mathbf{I}_{M_1} \otimes \dots \otimes \mathbf{K}_i^{(r)} \otimes \dots \otimes \mathbf{I}_{M_R} \right), \quad i = 1, 2.$$

The spatial frequencies $\hat{\mu}_i^{(r)}$ are derived from the eigenvalues $\hat{\omega}_i^{(r)}$ of the invariance matrix $\hat{\Upsilon}^{(r)}$ via the nonlinear mapping:

$$\hat{\mu}_i^{(r)} = 2 \cdot \arctan \left(\hat{\omega}_i^{(r)} \right), \quad i = 1, \dots, d.$$

The eigenvalues are computed using a joint eigendecomposition or a simultaneous Schur decomposition.

VI. SIMULATION RESULTS

In this section, we demonstrate the improvements introduced by the R -D tensorized NC approaches through simulations.

The root mean squared error (RMSE) serves as a critical metric for evaluating the accuracy of parameter estimation algorithms. For ESPRIT-based methods, the RMSE quantifies the average deviation between estimated spatial frequencies ($\hat{\mu}_i^{(r)}$) and their true values ($\mu_i^{(r)}$). The total RMSE across all R dimensions and d sources is defined as:

$$\text{RMSE} = \sqrt{\frac{1}{d} \sum_{i=1}^d \frac{1}{R} \sum_{r=1}^R \left(\hat{\mu}_i^{(r)} - \mu_i^{(r)} \right)^2}.$$

Furthermore, we compare our results with R -D standard Tensor ESPRIT (STE) [9], R -D unitary Tensor ESPRIT (UTE)

[10], R -D NC standard tensor ESPRIT (NC-STE) [17], R -D NC unitary tensor ESPRIT (NC-UTE) [17]. The proposed methods are denoted as R -D Tensorized NC Tensor ESPRIT (TNC-STE) and R -D Tensorized NC Unitary Tensor ESPRIT (TNC-UTE). The simulation scenario shown in Fig. 1 consists of $d = 2$ uncorrelated sources that emit NC symbols with spatial frequencies $\mu_1^{(1)} = 1$, $\mu_2^{(1)} = 0.95$, $\mu_1^{(2)} = 1$, $\mu_2^{(2)} = 0.95$, and $\mu_1^{(3)} = 1$, $\mu_2^{(3)} = 0.95$. The rotation phases $\text{diag}\{\Psi\} = [\frac{\pi}{8}, \frac{5\pi}{8}]$.

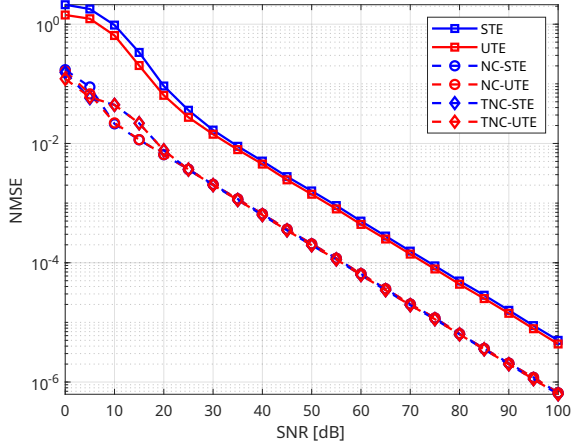


Fig. 1: Total RMSE of spatial frequencies versus the SNR for $R = 3$ -D array ($6 \times 6 \times 6$) and $d = 2$ sources at $\mu_1^{(1)} = 1$, $\mu_2^{(1)} = 0.95$, $\mu_1^{(2)} = 1$, $\mu_2^{(2)} = 0.95$, and $\mu_1^{(3)} = 1$, $\mu_2^{(3)} = 0.95$ with $N = 6$ snapshots and rotational phases $\text{diag}\{\Psi\} = [\frac{\pi}{8}, \frac{5\pi}{8}]$

Fig. 1 illustrates the performance comparison between several tensor-based ESPRIT algorithms. The results show that all NC algorithms significantly outperform their standard counterparts (STE/UTE), indicating the significant advantages of exploiting non-circularity in signal processing. While the proposed TNC-STE and TNC-UTE algorithms achieve comparable overall performance to NC-STE and NC-UTE, a slight performance gap is observed at lower SNR regimes. This marginal advantage of NC-STE/UTE in noise-dominated environments can be attributed to their repeated mode-wise HOSVD operations, which provide enhanced denoising capabilities in each tensor dimension independently. However, as the SNR increases, this advantage diminishes and all NC-based algorithms converge to similar performance levels.

Computational Complexity

The computational complexity of tensor-based ESPRIT algorithms is dominated by the Higher-Order Singular Value Decomposition (HOSVD), which scales with the tensor dimensions and the number of snapshots. Table I compares six variants, highlighting how the strict exploitation of NC source properties affects complexity and performance. Here we analyze the trade-offs between resolution and computational load for each of these methods.

TABLE I: Complexity Comparison of Tensor ESPRIT Algorithms

Algorithm	HOSVD Complexity
SE	$\mathcal{O}(N(\prod_r M_r)(N + \sum_r M_r))$
UE	$\mathcal{O}(\frac{N}{2}(\prod_r M_r)(N + \sum_r M_r))$
NC-SE	$\mathcal{O}(\sum_r 2M_r N \prod_{k \neq r} M_k (2M_r + N + \sum_{k \neq r} M_k))$
NC-UE	$\mathcal{O}(\frac{1}{2} \sum_r 2M_r N \prod_{k \neq r} M_k (\sum_{k \neq r} M_k + 2M_r + N))$
NC-STE	$\mathcal{O}(2N \prod_r M_r (N + 2 + \sum_r M_r))$
NC-UTE	$\mathcal{O}(N \prod_r M_r (N + 2 + \sum_r M_r))$

Where:

$$\prod_r M_r = \prod_{r=1}^R M_r, \sum_r M_r = \sum_{r=1}^R M_r$$

R : Number of dimensions, M_r : Sensors in dimension r , N : Snapshots

The baseline algorithms, STE and UTE, require a single HOSVD on the original measurement tensor. UTE reduces the complexity by 50% compared to STE by using real-valued transformations, thus avoiding complex arithmetic. However, both methods do not exploit the presence of non-circular sources, limiting their resolution. The NC extensions [10], [17] exploit non-circularity by doubling the virtual aperture along each of the R dimensions. This introduces R separate HOSVD operations, one for each extended dimension, resulting in complexity proportional to $\sum_r 2M_r \prod_{k \neq r} M_k$. For example, in a 3-D array ($R = 3$), NC-STE/UTE requires three HOSVDs on tensors of size $2M_1 \times M_2 \times M_3$, $M_1 \times 2M_2 \times M_3$, and $M_1 \times M_2 \times 2M_3$. While this improves resolution, the complexity grows linearly with R , becoming prohibitive for high-dimensional arrays.

The R -D Tensorized NC Tensor ESPRIT and R -D Tensorized NC Unitary Tensor ESPRIT algorithms consolidate non-circularity augmentation into a single mode (e.g., concatenation of original and conjugated measurements along a new dimension). This avoids R -fold HOSVD operations, instead performing a HOSVD on a tensor augmented along a unified mode. This significantly reduces the computational burden compared to NC-STE/UTE, while preserving the resolution benefits of strictly non-circular sources. For example, in a 3-D array, TNC-STE/UTE replaces three HOSVDs with a single HOSVD on a $M_1 \times M_2 \times M_3 \times 2N$ tensor, reducing complexity. By unifying non-circularity augmentation into a single mode, TNC-STE/TNC-UTE reduces computational complexity by $\frac{R-1}{R} \times 100\%$ compared to NC-STE/NC-UTE. This improvement is critical for high-dimensional arrays ($R \geq 3$), where traditional NC methods become impractical.

In Fig. 2 we show the result of the total computation time of the proposed methods based on the box plot visualization. The plot shows the distributions and mean execution times of different ESPRIT algorithm variants for the same scenario analyzed in Figure 1. The results show that the non-circular tensor variants (TNC-STE and TNC-UTE) have similar estimation performance compared to their non-circular counterparts in a standard non-circular setting (NC-STE and NC-UTE) at a significantly lower computational cost. The

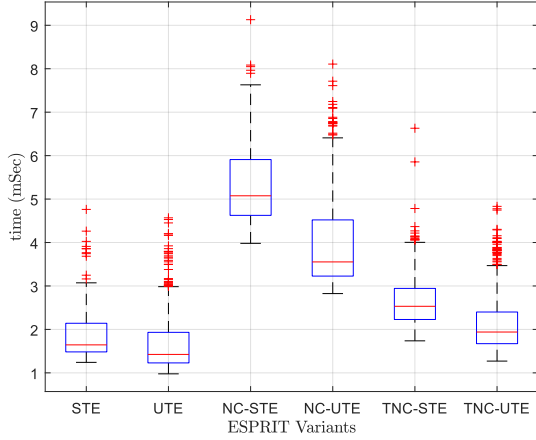


Fig. 2: Comparison of computational complexity of ESPRIT variants for a $(6 \times 6 \times 6)$ cubic uniform array and $d = 2$ sources at $\mu_1^{(1)} = 1, \mu_2^{(1)} = 0.95, \mu_1^{(2)} = 1, \mu_2^{(2)} = 0.95$, and $\mu_1^{(3)} = 1, \mu_2^{(3)} = 0.95$ with $N = 6$ snapshots and rotational phases $\text{diag}\{\Psi\} = [\frac{\pi}{8}, \frac{5\pi}{8}]$.

stable lower- and upper-quartile bounds of the tensor-based methods also show that the prediction time is more consistent and, as a result, may be more suitable for real-time systems with strict time constraints. These efficiency improvements are mainly due to the structured tensor representation and decomposition, which makes better use of multidimensional data relationships than traditional matrix-based methods.

VII. CONCLUSIONS

In this paper, we have discussed the R -D Tensorized NC Tensor ESPRIT and R -D Tensorized NC Unitary Tensor ESPRIT parametric estimation algorithms targeted at non-circular sources and R -D, shift-invariant arrays that are not necessarily centro-symmetric. The CP structure of the NC measurement tensor is leveraged in these algorithms to obtain high computational efficiency due to the unified multidimensional processing. This structural benefit minimizes redundant computations, notably avoiding repeated HOSVD operations, and provides an efficient estimation process. Nevertheless, the two approaches do not sacrifice any of their core advantages of strictly non-circular sources, such as their ability to resolve an increasing number of sources and their improved estimation accuracy relative to classical techniques. The Unitary variant (R -D Tensorized NC Unitary Tensor ESPRIT) improves the efficiency by converting complex-valued operations to real-valued operations, while not sacrificing estimation accuracy.

REFERENCES

[1] R. O. Schmidt, "Multiple emitter location and signal parameter estimation," *Proceedings of the IEEE Transactions on Antennas and Propagation*, vol. 34, no. 3, pp. 276–280, 1986.
[2] R. Roy and T. Kailath, "ESPRIT - estimation of signal parameters via rotational invariance techniques," *IEEE Transactions on Acoustics, Speech, and Signal Processing*, vol. 37, no. 7, pp. 984–995, 1989.

[3] C. Stoeckle, J. Munir, A. Mezghani, and J. A. Nosssek, "DOA estimation performance and computational complexity of subspace- and compressed sensing-based methods," in *19th International ITG Workshop on Smart Antennas*, 2015, pp. 1–6.
[4] A. Zoubir, P. Chargé, and Y. Wang, "Non circular sources localization with ESPRIT," in *Proc. European Conference on Wireless Technology (ECWT)*, Munich, Germany, Oct 2003.
[5] M. Haardt and F. Roemer, "Enhancements of Unitary ESPRIT for non-circular sources," in *Proceedings of the IEEE International Conference on Acoustics, Speech, and Signal Processing*, vol. 2, 2004, pp. ii–101.
[6] H. Abeida and J.-P. Delmas, "MUSIC-like estimation of direction of arrival for noncircular sources," *IEEE Transactions on Signal Processing*, vol. 54, no. 7, pp. 2678–2690, 2006.
[7] S. B. Hassen, F. Bellili, A. Samet, and S. Affes, "DOA estimation of temporally and spatially correlated narrowband noncircular sources in spatially correlated white noise," *IEEE Transactions on Signal Processing*, vol. 59, no. 9, pp. 4108–4121, 2011.
[8] J. Steinwandt, F. Roemer, C. Steffens, M. Haardt, and M. Pesavento, "Gridless super-resolution direction finding for strictly non-circular sources based on atomic norm minimization," in *Proceedings of the Asilomar Conference on Signals, Systems, and Computers*, 2016, pp. 1518–1522.
[9] M. Haardt, F. Roemer, and G. Del Galdo, "Higher-order SVD-based subspace estimation to improve the parameter estimation accuracy in multidimensional harmonic retrieval problems," *IEEE Transactions on Signal Processing*, vol. 56, no. 7, pp. 3198–3213, Jul. 2008.
[10] F. Roemer and M. Haardt, "Multidimensional Unitary tensor-ESPRIT for non-circular sources," in *Proceedings of the IEEE International Conference on Acoustics, Speech and Signal Processing*, 2009, pp. 3577–3580.
[11] C. Luo, Y. Changbo, and L. Baobao, "Computationally efficient ambiguity-free two-dimensional DOA estimation method for coprime planar array: Rd-root-MUSIC algorithm," *Sensors*, vol. 22, no. 7, p. 9325100, 2022.
[12] K. N. Mokios, N. D. Sidiropoulos, M. Pesavento, and C. E. Mecklenbrauker, "On 3-d harmonic retrieval for wireless channel sounding," in *Proceedings of the IEEE International Conference on Acoustics, Speech, and Signal Processing (ICASSP)*, vol. 2, 2004, pp. 89–92.
[13] M. Pesavento, C. F. Mecklenbrauker, and J. F. Boehme, "Multidimensional rank reduction estimator for parametric MIMO channel models," *EURASIP Journal on Applied Signal Processing*, pp. 1354–1363, Sep. 2004.
[14] M. Haardt and J. A. Nosssek, "Unitary ESPRIT: How to obtain increased estimation accuracy with a reduced computational burden," *IEEE Transactions on Signal Processing*, vol. 43, no. 5, pp. 1233–1242, 1995.
[15] L. D. Lathauwer, B. D. Moor, and J. Vandewalle, "On the best rank-1 and rank-(r_1, r_2, \dots, r_n) approximation of higher-order tensors," *SIAM J. Matrix Anal. Appl.*, vol. 21, no. 4, pp. 1324–1342, 2000.
[16] —, "A multilinear singular value decomposition," *SIAM J. Matrix Anal. Appl.*, vol. 21, no. 4, pp. 1253–1278, 2000.
[17] J. Steinwandt, F. Roemer, M. Haardt, and G. Del Galdo, "R-dimensional ESPRIT-type algorithms for strictly second-order non-circular sources and their performance analysis," *IEEE Transactions on Signal Processing*, vol. 62, no. 18, pp. 4824–4838, 2014.
[18] P. Tichavský, A.-H. Phan, and A. Cichocki, "Algorithms for Tensor factorization via low-rank approximations," in *Proceedings of the IEEE International Conference on Acoustics, Speech, and Signal Processing (ICASSP)*, Prague, Czech Republic, 2011, pp. 1–4.
[19] B. Sen and K. K. Parhi, "Constrained Tensor decomposition optimization with applications to fmri data analysis," in *Proceedings of the Asilomar Conference on Signals, Systems, and Computers*, 2018.

APPENDIX A

To derive $\mathcal{Z} = [\mathbf{y}^{(\text{nc})} \sqcup_{R+1} \mathbf{y}^{(\text{nc})} \times_{R+1} \mathbf{\Pi}_N]$, consider the following

$$\begin{aligned}
& \mathbf{y}^{(\text{nc})*} \times_{r=1}^R \mathbf{\Pi}_{M_r} \times_{R+2} \mathbf{\Pi}_2 \\
&= \left[\mathbf{y} \sqcup_{R+2} \mathbf{y}^* \times_{r=1}^R \mathbf{\Pi}_{M_r} \right]^* \times_{r=1}^R \mathbf{\Pi}_{M_r} \times_{R+2} \mathbf{\Pi}_2 \\
&= \left[\mathbf{y}^* \times_{r=1}^R \mathbf{\Pi}_{M_r} \sqcup_{R+2} \mathbf{y} \right] \times_{R+2} \mathbf{\Pi}_2 \\
&= \left[\mathbf{y}^* \times_{r=1}^R \mathbf{\Pi}_{M_r} \sqcup_{R+2} \mathbf{y} \right] \times_{R+2} \begin{bmatrix} 0 & 1 \\ 1 & 0 \end{bmatrix} \\
&= \mathbf{y}^* \times_{r=1}^R \mathbf{\Pi}_{M_r} \times_{R+2} \begin{bmatrix} 0 \\ 1 \end{bmatrix} + \mathbf{y} \times_{R+2} \begin{bmatrix} 1 \\ 0 \end{bmatrix}, \text{ (Using eqn. (2))} \\
&= \left[\mathbf{0} \sqcup_{R+2} \mathbf{y}^* \times_{r=1}^R \mathbf{\Pi}_{M_r} \right] + \left[\mathbf{y} \sqcup_{R+2} \mathbf{0} \right] \text{ (eqn. (3))} \\
&= \mathbf{y}^{(\text{nc})}.
\end{aligned}$$

Substituting above result in the definition of \mathcal{Z} , we get

$$\begin{aligned}
\mathcal{Z} &= \left[\mathbf{y}^{(\text{nc})} \sqcup_3 \mathbf{y}^{(\text{nc})*} \times_{r=1}^R \mathbf{\Pi}_{M_r} \times_{R+1} \mathbf{\Pi}_N \times_{R+2} \mathbf{\Pi}_2 \right] \\
&= \left[\mathbf{y}^{(\text{nc})} \sqcup_{R+1} \mathbf{y}^{(\text{nc})} \times_{R+1} \mathbf{\Pi}_N \right].
\end{aligned}$$

APPENDIX B

The real-valued transformation of \mathcal{Z} is

$$\varphi(\mathcal{Z}) = \left(\mathcal{Z} \times_r \mathbf{Q}_{M_r}^H \right) \times_{R+1} \mathbf{Q}_{2N}^H \times_{R+2} \mathbf{Q}_2^H, \quad (25)$$

Firstly, let us consider a part of eqn. (25) as

$$\left(\mathcal{Z} \times_r \mathbf{Q}_{M_r}^H \right) \times_{R+2} \mathbf{Q}_2^H.$$

Using the definition of \mathcal{Z} (Appendix A) and $\mathbf{y}^{(\text{nc})}$ (eqn. (12)), this becomes

$$\begin{aligned}
& \mathcal{Z} \times_r \mathbf{Q}_{M_r}^H \times_{R+2} \mathbf{Q}_2^H \\
&= \left[\left[\mathbf{y} \sqcup_{R+2} \tilde{\mathbf{y}} \right] \sqcup_{R+1} \left[\mathbf{y} \sqcup_{R+2} \tilde{\mathbf{y}} \right] \times_{R+1} \mathbf{\Pi}_N \right] \\
& \quad \times_{r=1}^R \mathbf{Q}_{M_r}^H \times_{R+2} \mathbf{Q}_2^H, \quad (26)
\end{aligned}$$

where $\tilde{\mathbf{y}} = \mathbf{y}^* \times_{r=1}^R \mathbf{\Pi}_{M_r}$.

Consider $\mathcal{Q} = \mathbf{y} \times_r \mathbf{Q}_{M_r}^H \times_{R+2} \mathbf{Q}_2^H$ then it follows as

$$\tilde{\mathbf{y}} \times_r \mathbf{Q}_{M_r}^H = \mathbf{y} \times_r \mathbf{Q}_{M_r}^H \mathbf{\Pi}_{M_r} = \mathcal{Q}^*. \quad (27)$$

Substituting eqn. (27) in (26),

$$\begin{aligned}
& \mathcal{Z} \times_r \mathbf{Q}_{M_r}^H \\
&= \left[\left[\mathcal{Q} \sqcup_{R+2} \mathcal{Q}^* \right] \sqcup_{R+1} \left[\mathcal{Q} \sqcup_{R+2} \mathcal{Q}^* \right] \times_{R+1} \mathbf{\Pi}_N \right] \\
& \quad \times_{r=1}^R \mathbf{Q}_{M_r}^H \times_{R+2} \mathbf{Q}_2^H \\
&= \left[\left[\mathcal{Q} \sqcup_{R+2} \mathcal{Q}^* \right] \sqcup_{R+1} \right. \\
& \quad \left. \left[\mathcal{Q} \sqcup_{R+2} \mathcal{Q}^* \right] \times_{R+1} \mathbf{\Pi}_N \right] \times_{R+2} \mathbf{Q}_2^H \\
&= \left[\left[\mathcal{Q} \sqcup_{R+2} \mathcal{Q}^* \right] \times_{R+2} \mathbf{Q}_2^H \sqcup_{R+1} \right. \\
& \quad \left. \left[\mathcal{Q} \sqcup_{R+2} \mathcal{Q}^* \right] \times_{R+1} \mathbf{\Pi}_N \times_{R+2} \mathbf{Q}_2^H \right] \quad (28)
\end{aligned}$$

Consider a part of above eqn. (28)

$$\begin{aligned}
& \left[\mathcal{Q} \sqcup_{R+2} \mathcal{Q}^* \right] \times_{R+2} \mathbf{Q}_2^H \\
&= \left[\mathcal{Q} \sqcup_{R+2} \mathcal{Q}^* \right] \times_{R+2} \begin{bmatrix} 1 & 1 \\ -j & j \end{bmatrix} \\
&= \mathcal{Q} \times_{R+2} \begin{bmatrix} 1 \\ -j \end{bmatrix} + \mathcal{Q}^* \times_{R+2} \begin{bmatrix} 1 \\ j \end{bmatrix} \text{ Using eqn. (1)} \\
&= \left[\mathcal{Q} \sqcup_{R+2} -j\mathcal{Q} \right] + \left[\mathcal{Q}^* \sqcup_{R+2} j\mathcal{Q}^* \right] \\
&= \left[\text{Re} \{ \mathcal{Q} \} \sqcup_{R+2} \text{Im} \{ \mathcal{Q} \} \right] \quad (29)
\end{aligned}$$

Substituting above result in eqn. (28)

$$\mathcal{Z} \times_r \mathbf{Q}_{M_r}^H \times_{R+2} \mathbf{Q}_2^H = \left[\mathcal{P} \sqcup_{R+1} \mathcal{P} \times_{R+1} \mathbf{\Pi}_N \right],$$

where $\mathcal{P} = \left[\text{Re} \{ \mathcal{Q} \} \sqcup_{R+2} \text{Im} \{ \mathcal{Q} \} \right]$. Finally, substituting $\mathcal{Z} \times_r \mathbf{Q}_{M_r}^H \times_{R+2} \mathbf{Q}_2^H$ in eqn. (25) to complete the real-valued transformation as

$$\begin{aligned}
\varphi(\mathcal{Z}) &= \left(\mathcal{Z} \times_r \mathbf{Q}_{M_r}^H \times_{R+2} \mathbf{Q}_2^H \right) \times_{R+1} \mathbf{Q}_{2N}^H \\
&= \left[\mathcal{P} \sqcup_{R+1} \mathcal{P} \times_{R+1} \mathbf{\Pi}_N \right] \times_{R+1} \mathbf{Q}_{2N}^H \\
&= \left[\mathcal{P} \sqcup_{R+1} \mathcal{P} \times_{R+1} \mathbf{\Pi}_N \right] \times_{R+1} \begin{bmatrix} \mathbf{I}_N & \mathbf{\Pi}_N \\ -j\mathbf{I}_N & j\mathbf{\Pi}_N \end{bmatrix} \\
&= \left[\mathcal{P} \times_{R+1} \begin{bmatrix} \mathbf{I}_N \\ -j\mathbf{I}_N \end{bmatrix} + \mathcal{P} \times_{R+1} \mathbf{\Pi}_N \times_{R+1} \begin{bmatrix} \mathbf{\Pi}_N \\ j\mathbf{\Pi}_N \end{bmatrix} \right] \\
&= \left[\mathcal{P} \times_{R+1} \begin{bmatrix} \mathbf{I}_N \\ -j\mathbf{I}_N \end{bmatrix} + \mathcal{P} \times_{R+1} \begin{bmatrix} \mathbf{I}_N \\ j\mathbf{I}_N \end{bmatrix} \right] \\
&= \left[\mathcal{P} \sqcup_{R+1} \mathbf{0} \right] \\
&= \left[\left[\text{Re} \{ \mathcal{Q} \} \sqcup_{R+2} \text{Im} \{ \mathcal{Q} \} \right] \sqcup_{R+1} \mathbf{0} \right]. \quad (30)
\end{aligned}$$

Thus the real-valued transformation of \mathcal{Z} is given as $\left[\text{Re} \{ \mathcal{Q} \} \sqcup_{R+2} \text{Im} \{ \mathcal{Q} \} \right]$ where, $\mathcal{Q} = \mathbf{y} \times_r \mathbf{Q}_{M_r}^H$.